We are IntechOpen,
the world's leading publisher of Open Access books
Built by scientists, for scientists

6,900
Open access books available

186,000
International authors and editors

200M
Downloads

154
Countries delivered to

Our authors are among the

TOP 1%
most cited scientists

12.2%
Contributors from top 500 universities

WEB OF SCIENCE™

Selection of our books indexed in the Book Citation Index
in Web of Science™ Core Collection (BKCI)

Interested in publishing with us?
Contact book.department@intechopen.com

Numbers displayed above are based on latest data collected.
For more information visit www.intechopen.com

Non-Intrusive Characterization and Monitoring of Fluid Mud: Laboratory Experiments with Seismic Techniques, Distributed Acoustic Sensing (DAS), and Distributed Temperature Sensing (DTS)

Deyan Draganov, Xu Ma, Menno Buisman, Tjeerd Kiers, Karel Heller and Alex Kirichek

Abstract

In ports and waterways, the bathymetry is regularly surveyed for updating navigation charts ensuring safe transport. In port areas with fluid-mud layers, most traditional surveying techniques are accurate but are intrusive and provide one-dimensional measurements limiting their application. Current non-intrusive surveying techniques are less accurate in detecting and monitoring muddy consolidated or sandy bed below fluid-mud layers. Furthermore, their application is restricted by surveying-vessels availability limiting temporary storm- or dredging-related bathymetrical changes capture. In this chapter, we first review existing non-intrusive techniques, with emphasis on sound techniques. Then, we give a short review of several seismic-exploration techniques applicable to non-intrusive fluid-mud characterization and monitoring with high spatial and temporal resolution. Based on the latter, we present recent advances in non-intrusive fluid-mud monitoring using ultrasonic transmission and reflection measurements. We show laboratory results for monitoring velocity changes of longitudinal and transverse waves propagating through fluid mud while it is consolidating. We correlate the velocity changes with shear-strength changes while the fluid mud is consolidating and show a positive correlation with the yield stress. We show ultrasonic laboratory results using reflection and transmission techniques for estimating the fluid-mud longitudinal- and transverse-wave velocities. For water/mud interface detection, we also use distributed acoustic sensing (DAS) and distributed temperature sensing (DTS).

Keywords: Safe navigation, non-intrusive monitoring of fluid mud, transmission seismic measurements, reflection seismic measurements, yield stress, distributed acoustic sensing (DAS), distributed temperature sensing (DTS)

1. Introduction

Safe navigation through fluid mud is increasingly important because enhancing the navigability with less dredging can help lower transportation costs and benefit biodiversity. The areas with fluid-mud layers need to be routinely surveyed to provide navigation charts used by the vessels. Fluid mud is described as a highly concentrated non-Newtonian suspension of sediment consisting mainly of water, organic matter, silt and clay minerals [1]. Fluid mud is a crucial factor when determining the nautical depth (nautical bottom). It is typically defined by a density value [2]. For example, the Port of Rotterdam uses the density of 1.2 kg/L as a nautical-depth criterium. Other parameters are though also used – for example, the Port of Emden adopts the yield stress of 100 Pa to define the nautical depth [2, 3]. Thus, it is important to have an accurate parameter that description of the fluid mud and could be used in the same way in different ports.

Full-scale and scaled experiments for safe ship navigation in the ports and waterways have been performed already for several decades [3–5]. Traditional ways of characterizing fluid mud involve its sampling, which inevitably disturbs the mud. Other methods, for instance radioactive probes, such as X- and γ-ray tube, can be used to measure the density of the fluid mud, where the density calculation is based on the Lambert–Beer Law [6]. The density profiler based on X-rays – DensX, and the Graviprobe, which measures the cone-penetration resistance and pressures when sinking freely in the water-mud column, can be used to estimate the density and undrained shear strength, respectively [7, 8]. Although these tools can provide a quantitative information about the densities and strength of mud, non-intrusive characterization and monitoring of fluid mud in ports and waterways is preferable. Currently, echo-sounding measurements are used as non-intrusive techniques for assessment of the nautical depth, for which the relationship between the acoustic impedance and densities of the fluid mud are investigated [9]. Multi-beam echo-sounders are deployed to detect fluid-mud layers. Utilization of signals at a higher frequency (200–215 kHz) and at a lower frequency (15–40 kHz) provides an estimate of the approximate thickness of the fluid-mud layer [7]. The higher-frequency measurements are used to map the lutocline, while the lower-frequency measurements provide an estimate of the sea-floor depth. Schrottke and Becker deployed a high-resolution side-scan sonar with a frequency of 330 kHz and a parametric sub-bottom profiler with frequencies of about 100 kHz for detecting the fluid mud with high vertical resolution [10]. The velocimeter, especially the acoustic Doppler velocimeter, was developed on the basis of ultrasonic waves to measure turbulency velocities in the fluid-mud sediments [11]. The mentioned techniques, though, rely on longitudinal (P-) waves, which are related to the bulk properties of the materials.

The propagation velocity and amplitude of transverse (S-) waves strongly depend on the geotechnical properties of the sediment, such as fluid mud [12]. Thus, S-waves could be used to characterize the fluid mud more precisely than when using P-waves and thus bulk properties. However, in seismic exploration in marine environments, the sources and receivers are usually deployed in the water column, more often relatively close to the water surface. Thus, the sources, such as airgun arrays, give rise to P-waves, and the receivers, usually towed by a vessel as streamers, record P-waves as well. This limits the utilization of S-waves because extracting the S-wave information is rather more involving and time-consuming [12]. Still, strong P-to-S-converted waves could be generated at the water bottom, and their utilization for characterization of the fluid mud is possible. A technique that could allow direct extraction of the S-wave velocities is seismic interferometry (SI) for retrieval of non-physical reflections. SI is a method that retrieves new recordings from existing recordings most often by cross-correlation [13–15] of the

existing recordings. When the required assumptions for the practical application of SI are not met, non-physical arrivals are also retrieved. Some of the non-physical arrivals arise from internal reflections between layer boundaries [16–18]. SI can thus be applied for targeted retrieval specifically of non-physical (ghost) reflections to estimate the layer-specific velocities for layers in the subsurface [17, 18].

Ultrasonic transmission measurements of marine sediments have been performed, and it was reported that the P-wave attenuation coefficients indicate changes in the sediment composition more distinctly than the velocity of the P-waves [19]. Additionally, relationships between the porosity and P- and S-waves velocities were examined [19]. Leurer [20] carried out pulse-transmission measurements with a center frequency of 50 kHz and reported that in a foraminiferal mud the P-wave velocities range between 1840 m/s and 2462 m/s. Using a center frequency of 100 kHz under different effective pressures, it was also found that the S-wave velocities range between 450 m/s and 975 m/s [20]. Other studies showed that the S-wave velocity in mud samples can be as low as 7 m/s when using signals with a center frequency of 200 Hz [21, 22]. These different values for the P- and S-wave velocities show that it is necessary to perform seismic (ultrasonic) measurements for characterization of the fluid mud for each specific location, i.e., for each port or waterway. This would favor utilization of reflection measurements like in seismic exploration as they can be performed more easily. Additionally, seismic reflection experiments can be conducted with the aid of synthetic seismogram analysis to investigate the shear-wave velocity structure of the shallow-water sediments [23].

Seismic measurements for characterization and monitoring of the subsurface targets are also performed by means of distributed acoustic sensing (DAS) and with distributed temperature sensing (DTS). DAS has already been successfully used in the field of earthquake seismology [24–28], vertical seismic profiling [29, 30], and ambient noise velocity inversions [31]. DTS measurements have been used for monitoring of subsea structures [32] and of carbon capture, utilization and storage [33]. Thus, DAS and DTS could also be very useful in for characterization of fluid mud.

Utilization of DAS and DTS to measure seismic waves in the water and fluid mud offers advantages over the conventional electrical sensors such as electric isolation, immunity to electromagnetic interference, but also that they are non-conductive and non-corrosive, making them well-suited with regard to safety and durability for utilization in liquid-level sensing [34–37]. Such practical advantages are complemented by economical ones. There has been a rapid development in the optical fibers due to their wide usage by the communication industry. This has led to a substantial decrease in price, as well as an increase in performance. For instance, a single-mode optical fiber that used to cost $ 20$/m in 1979 costed just 0.1 $/m in 2008 [38]. Given that the optical fibers are relatively cheap and require little to no maintenance, they could be very useful, from an economical point of view, as receivers for monitoring the nautical depth in ports and waterways. With the experiments we describe below, we investigate the utilization of optical fibers as receivers for fluid-mud level detection and characterization.

In the following, we use laboratory ultrasonic experiments to investigate how P- and S-wave measurements can be used for fluid-mud characterization. We discuss the latest results of seismic (ultrasonic) measurements of P- and S-waves propagation through fluid mud. In Section 2, we first describe the materials, sample preparation, and the rheological experiments for measuring the yield stress. We then introduce the ultrasonic measurements systems we use for transmission and reflection measurements. Subsequently, we describe the DAS and DTS measurement setups.

In Section 3, we present the results from the transmission measurements for monitoring possible changes of the P- and S-wave velocities when the ultrasonic signals propagate through fluid mud at different stages of consolidation. We link

the observed transmission velocity changes to the measured yield stress during the same consolidation stages of the fluid mud. Further, we describe results from the reflection setup for estimating the layer-specific P- and S-wave velocities of the fluid mud. Finally, we validate the utilization of DAS and DTS as seismic and temperature receivers in laboratory experiments for detecting the fluid-mud/water interface.

In Section 4, we discuss the accuracy of our results and their applicability to other ports, while in Section 5 we draw conclusions.

2. Characterization and monitoring of fluid mud in a laboratory

We develop laboratory ultrasonic measurement systems for transmission and reflection seismic measurements for characterization and monitoring of fluid mud while it is consolidating. The transmission seismic-measurements systems are designed for direct, fast, point-to-point measurements in the fluid mud using ultrasonic transducers or DAS as receivers. The reflection seismic-measurements system uses ultrasonic transducers to record waves that have reflected or refracted at different layer boundaries including the bottom of the water layer and the bottom of the fluid-mud layer. The reflection measurements can be used to record common-source gathers, which can subsequently be utilized to characterize velocity changes in the fluid mud during the consolidation using seismic-exploration techniques. We also describe the laboratory setup for rheological measurements of the fluid mud and the setup for DTS measurements.

2.1 Fluid-mud sample preparation and handling

For the transmission and reflection measurements, we use fluid-mud samples extracted from the Calandkanaal (Port of Rotterdam) at the location indicated in **Figure 1a**. Before conducting the measurements, we stir a sample using a mechanical mixer in order to obtain a homogeneous volume of fluid mud with a uniform density. The density of the homogenized sample is 1197 kg/m3. After the homogenization, the fluid-mud sample appears like a mud slurry (**Figure 1b**). The samples are consecutively left to consolidate through a self-weight process. We perform ultrasonic measurements while the fluid mud is consolidating. Synchronously with the ultrasonic measurements, we also perform rheological measurements to investigate the yield stress. We investigate the fluidic yield stress using a recently

Figure 1.
(a) Map of the port of Rotterdam illustrating the location of the site from where the fluid-mud samples had been collected (source: Google maps). (b) The process of homogenizing fluid mud with a mechanical mixer.

developed protocol for the fluid mud [39, 40]. We use a HAAKE MARS I rheometer (Thermo Scientific) with two measuring geometries (Couette and vane) and apply stress ramp-up tests to measure the yield stress. The stress ramp-up tests are performed using a stress increase from 0 to 500 Pa at a rate of 1 Pa/s, until the shear rate reaches 300 s^{-1}, under a stress-control mode.

2.2 Transmission seismic measurements with transducer receivers

The transmission seismic laboratory setup is equipped with two pairs of piezo-electric ultrasonic transducers (**Figure 2b** and **c**). Each pair consists of a source and receiver transducer, with one of the pairs using P-wave transducers and the other pair – S-wave transducers. The direct transmission measurement represents a point-to-point measurement with both transducer pairs placed along the horizontal direction. Because of this source-receiver geometry, the estimated velocities of the P- and S- waves correspond to transmissions along horizontal layers inside the fluid mud, if such layers are developed.

As shown in **Figure 2a**, the laboratory setup includes a fluid-mud tank, a signal-control part, and the two pairs of ultrasound transducers. The signal-control part in turn consists of a source-control part and a receiver-control part. In the source-control part, a function generator produces a desired signal, which signal is subsequently passed to a power amplifier to be finally passed to the source transducer, which sends it through the fluid mud. The fluid-mud tank is a plastic box that has
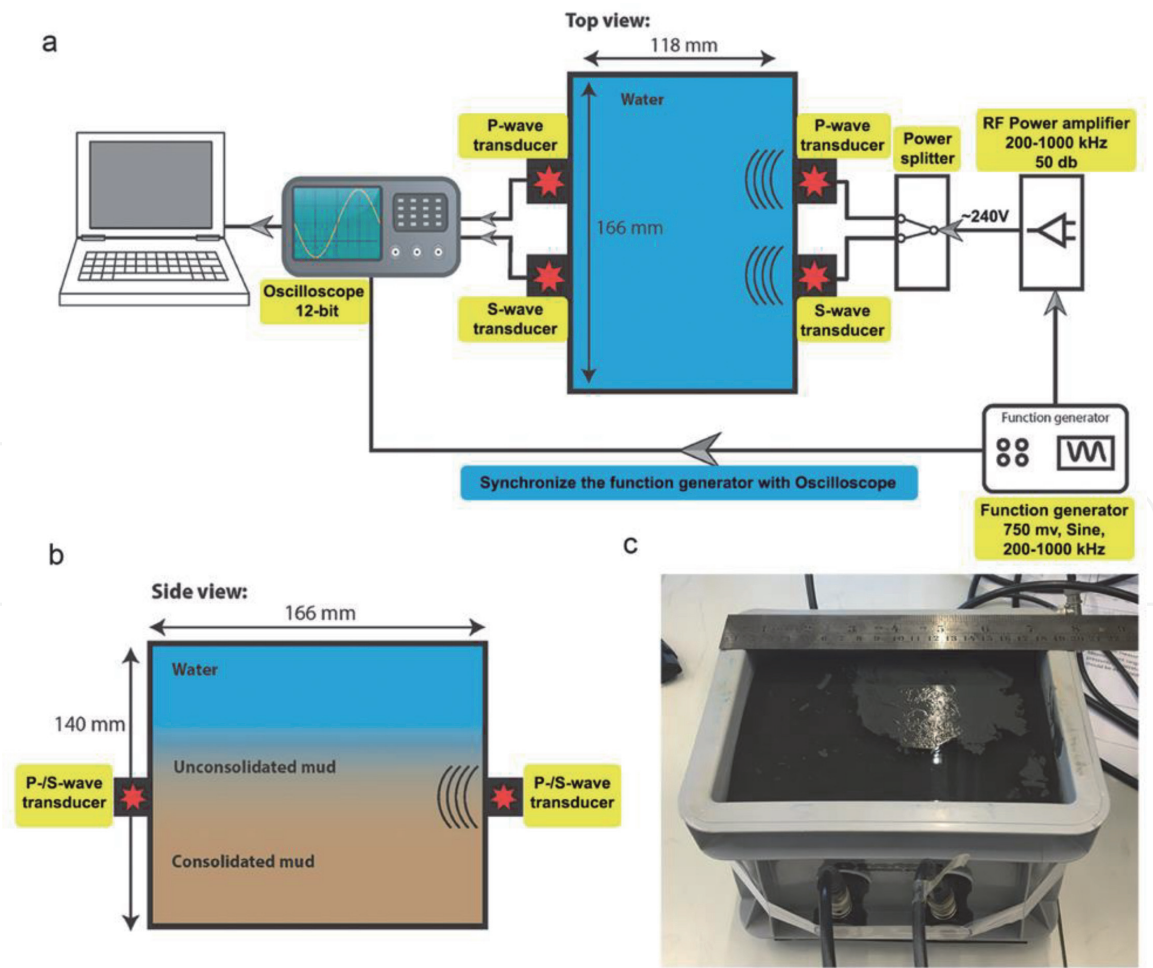

Figure 2.
(a) Sketch of the transmission seismic laboratory setup with the fluid-mud box viewed from above and showing the horizontal arrangement of the two transducer pairs. (b) Side view of the fluid-mud box showing the vertical alignment of the ultrasonic transducers. (c) Photo of the fluid-mud box showing also the two source transducers.

opening for the installation of the transducer end-caps. The receiver-control part of the setup consists of the receiver transducers, attached to the fluid-mud tank using end-caps, an oscilloscope for digitalization and displaying, and a computer, connected to the oscilloscope, to record the sensed signals. The generated source signal is also visualized on the oscilloscope for quality control.

For the transmission measurements, we use as a source signal a gated sine-wave pulse with a center frequency of 1 MHz. A measurement is performed using a pulse-time delay. To increase the signal-to-noise ratio, especially needed for the S-wave velocity estimations, a measurement at each stage of consolidation consists of 1024 repeated recordings summed together to obtain a final transmission recording. This is done for both the P- and S-wave pair.

For each stage of the measurements, the first step in estimating the propagation velocities is to pick the first arrivals of the P- and S-waves. The second step is to calculate the P- and S-wave velocities by dividing the travel distance of waves, which is the distance from the source to the receiver transducer within each pair (equal for both pairs), by the travel times estimated from the picked first arrivals.

2.3 Reflection seismic measurements with transducer receivers

Similar to the transmission seismic laboratory setup, the reflection system consists of a signal-control part, a fluid-mud tank, and ultrasound transducers, but further to that also includes a transducer-placement part (**Figure 3**). While the signal-control part is the same as for the transmission measurements (**Figure 3b**), the fluid-mud tank is different and only one pair of ultrasonic transducers is used (**Figure 3c**). The transducer-placement part allows changing the positions of the transducers by moving them along horizontal and vertical bars (**Figure 3a** and **c**). This facilitates recording of reflections at multiple horizontal positions to obtain reflection common-source gathers, if desired with sources and receivers at different depths.

In the measurements we perform, the transducers are placed a certain distance above the top of the fluid-mud layer to better mimic a geometry of a marine seismic-exploration survey. While placing sources and receivers during a field measurement campaign directly at the top of the fluid mud would allow direct recording of S-waves, a recording geometry with seismic sources and receivers towed at a certain height above the bed in the navigational channel is more practical – the surface of the sediments is seldomly flat, and hard object protruding from the sediments could damage the sources and/or receivers. On the other hand, towing the sources and receivers at a distance above the top of the fluid-mud layer inevitably brings uncertainty in the estimated seismic velocities caused by the salinity and temperature of the water. It is possible to monitor the changes in the salinity and temperature at specific locations, but the uncertainty still remains when using such point measurements for larger-area surveys due to the dynamics of the marine environments.

In order to eliminate these uncertainties, we apply SI for retrieval of ghost reflections from inside the fluid-mud layer and eliminate the travel-paths of the waves in the water layer. For pressure measurements in water, like in our laboratory setup, a general representation of SI by cross-correlation is [41].

$$p(R2, R1, t) + p(R2, R1, -t) \propto \sum_{S=S1}^{SN} p(R2, S, t) \otimes p(R1, S, t), \qquad (1)$$

where $p(R2, R1, t)$ is the retrieved pressure response at receiver at $R2$ from a virtual source at the position of a receiver at $R1$, $p(R2, S, t)$ is the pressure response measured at $R2$ from a source at S, with $S1 \ldots SN$ sources distributed evenly over
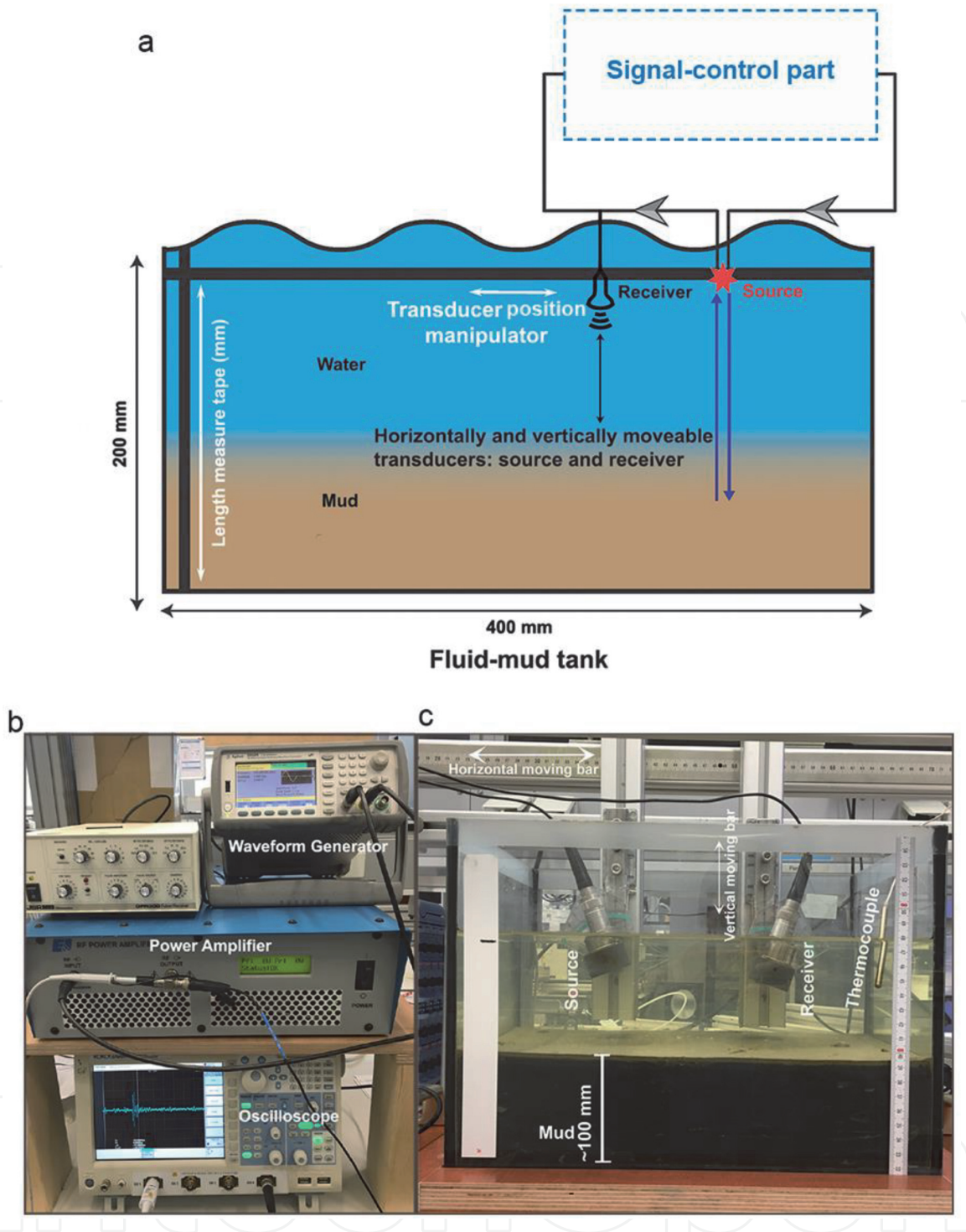
Figure 3.
Reflection seismic-measurements system. (a) Cartoon of the fluid-mud tank with the transducer-placement part and the signal-control part (identical to the one in the transmission measurements). Red star indicates the source and black probe indicates the receiver. The transducer-placement part allows vertical (blue arrows) and horizontal (white arrows) displacement of the source and receiver. (b) Photo of the signal-control part. (c) Photo of the fluid-mud tank and the transducer-placement part with a source and receiver ultrasonic transducers.

surface that effectively surrounds the two receivers, $-t$ indicates time reversal (acausal time), and $\otimes$ indicates correlation. As mentioned above, when the assumptions for this simplified representation are not met [14], e.g. as in a seismic reflection survey when the sources are only at the surface and thus do not surround the receivers, ghost reflections are retrieved [17, 18], and we can write

$$p(R2, R1, t) + p(R2, R1, -t) + ghosts \propto \sum_{S=SK1}^{SK2} p(R2, S, t) \otimes p(R1, S, t), \qquad (2)$$

where *ghosts* represents retrieved non-physical arrivals, including ghost reflections, and $SK1$ and $SK2$ now indicate that the summation is only over sources on a limited surface. For practical purposes, in our laboratory setup we choose to have only two source positions and multiple receiver positions. Using source-receiver reciprocity, we can thus rewrite relation (2) as

$$p(S2, S1, t) + p(S2, S1, -t) + ghosts \propto \sum_{R=RK1}^{RK2} p(S2, R, t) \otimes p(S1, R, t), \qquad (3)$$

where the summation is now over receiver positions and we retrieve a pressure recording at a virtual receiver at the position of source $S2$ from a sourse at $S1$. Thus, to apply SI, we use two common-source gathers (CSGs). The two source positions (labeled Source 1 or S1 and Source 2 or S2 in **Figures 4** and **5**, respectively) at the same height and distanced in the horizontal direction 50 mm from each other. We record the reflected signal at a receiver, labeled Receiver 1 (R1) in **Figure 4**, aligned with the two source positions and distanced 100 mm from S1 (and thus 50 mm from S2). Following the nomenclature in [17], the source and virtual receiver redatumed by SI to the top of the fluid-mud layer during the ghost-reflection retrieval are referred to as ghost source and ghost receiver, respectively. Assuming a favorable geometry, to explain the retrieval of a ghost reflection inside the fluid-mud layer, the travel-path of the reflection from the fluid-mud bottom, i.e., the travel-path starting from S1, transmitted at the water/mud interface, reflected by the fluid-mud bottom, transmitted at the mud/water interface, and then arriving at R1 is labeled 1–2–3-4 in **Figure 4**. The travel-path of the reflection from the water/mud interface, starting from S2 and arriving at R1, is labeled 1'-4'. Cross-correlation of the recorded reflections at R1 from S1 and S2 will effectively result in removal of the common travel-paths in 1–2–3-4 and 1'-4'. Thus, the parallel travel-paths 1 and 1' and the coinciding travel-paths 4 and 4' are eliminated, and only the travel-path 2–3 is left over representing a ghost reflection only inside the fluid-mud layer from a ghost source and ghost receiver placed directly at its top (**Figure 4**). In reality, the exact receiver position ensuring that travel-paths 1 = 1' and 4 = 4' is unknown. Because of that, recordings at multiple receiver positions from both sources are required, i.e., two CSGs. To obtain such gathers, we displace the receiver from position R1 to the right along the horizontal bar by 5 mm multiple times and record
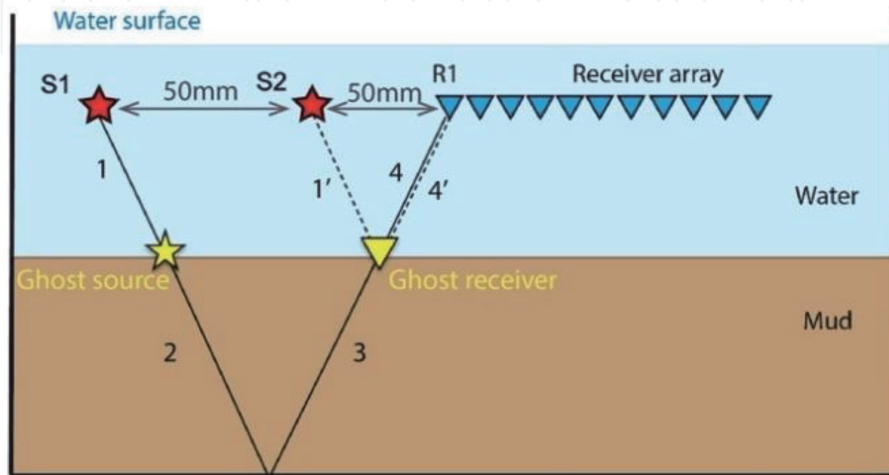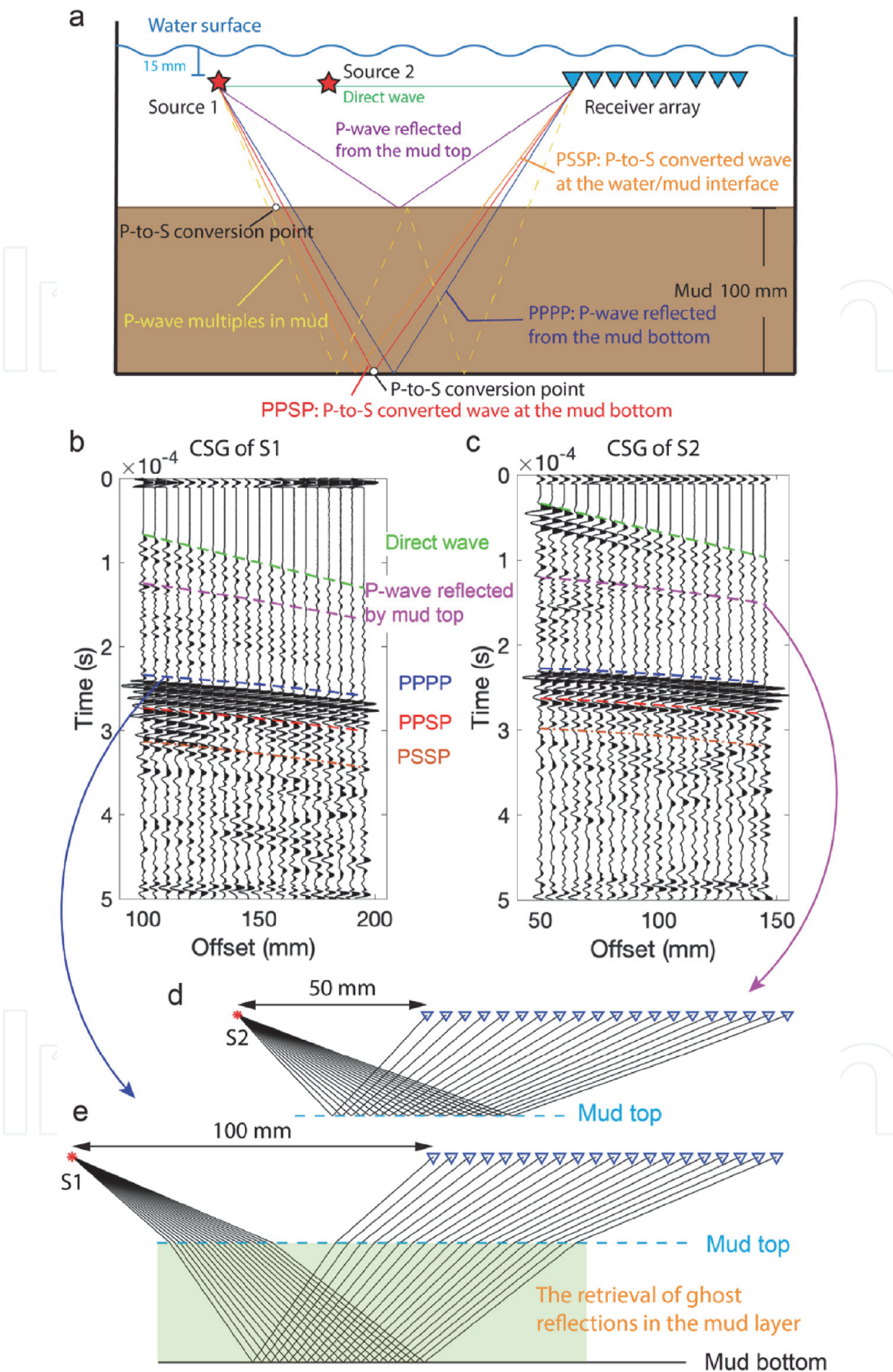

Figure 4.
Illustration of the geometry needed for retrieval of ghost reflections from inside the fluid-mud layer. See text for explanation of the symbols.

Figure 5.
(a) Illustration of the travel-paths of the expected arrivals from S1 to a receiver in the reflection measurements. (b) Wiggle plot of the recorded CSG from S1. (c) Wiggle plot of the recorded CSG from S2. (d) Sketch of the travel-paths of the primary reflections of the mud top in the CSG from S2. (e) Sketch of the travel-paths of the primary reflection of the mud bottom (PPPP) in the CSG from S1. The ghost reflection is retrieved by summing the individual arrivals highlighted in green in (e) obtained from cross-correlating the primary reflection from the fluid-mud top in the CSG from S2 with the primary reflection PPPP in the CSG from S1.

for the same source at each receiver position. In this case, we record at 20 positions. That is, the CSGs for S1 and S2 consist of 20 traces each.

The source signal we use is similar to the one for the transmission measurements but with a center frequency of 100 kHz.

Also with these measurements, to increase the signal-to-noise ratio of the recorded signals, a measurement at each receiver position from each source is repeated 1024 times and the 1024 measurements are summed together to obtain a final trace for that source and receiver positions.

Using the travel-path sketches in **Figure 5a**, we explain several arrivals of interest in the CSGs. **Figure 5b** and **c** present wiggle plots of the recorded CSGs from S1 and S2, respectively. We calculate expected arrival times based on the source/receiver offsets and the thicknesses of the water and fluid-mud layers, each of which we can directly measure. For propagation through the water layer, we use P-wave velocity of 1500 m/s. For the waves propagating through the fluid mud, we use values estimated from the transmission measurements – 1570 m/s for the P-wave velocity and 958 m/s for the S-wave velocity. The calculated reference times are illustrated by dashed lines superimposed on the CSGs to assist in interpretation of the arrivals. In **Figure 5b** and **c**, the reflection arrivals of interest in this study are the primary reflection from the fluid-mud top (magenta) and the three primary reflections from the fluid-mud bottom that are labeled as PPPP (blue), PPSP (red), and PSSP (orange). The S-waves in the experiment appear as waves converted from P to S at the top or the bottom of the fluid-mud layer. For example, the P-to-S converted wave in PPSP is generated when the P-wave impinging on the fluid-mud bottom is reflected as an S-wave; the P-to-S converted wave in PSSP is generated when the P-wave impinging on the fluid-mud top in transmitted to the fluid mud as an S-wave (**Figure 5a**) and continues to propagate as an S-wave until reaching the fluid-mud top again.

To retrieve ghost reflections, one can use relation (3) and correlate the CSGs. Such an approach could result in other retrieved arrivals interfering with the desired ghost reflections. To avoid that, we follow [17] and correlate only specific arrivals. To retrieve a P-wave ghost reflection from inside the fluid mud, we cross-correlate the primary reflection from the fluid-mud top in the CSG from S2 (**Figure 5d**) with the primary reflection PPPP in the CSG from S1 (**Figure 5e**). In a similar way, the P-to-S converted ghost reflection and S-wave ghost reflection are retrieved using the reflections PPSP and PSSP in the CSG from S1, respectively.

2.4 Transmission seismic measurements using DAS and measurements with DTS

We use a standard single-mode communication fiber for both the DAS and DTS measurements. This means that we can combine the two methods and compare the difference in their performance With DAS, such fibers can act as seismic receivers that measure the dynamics of a strain field acting on a fiber [42]. With DTS, such fibers can act as strain and temperature sensors (and thus also labeled DT(S)S), which measure the static strain and temperature along the fiber [43].

To verify that these fibers can serve as receivers for fluid-mud level detection and characterization, we conduct seismic and temperature laboratory experiments using commercially available interrogators. These interrogators are the iDAS from Silixa and DITEST STA-R from Omnisens for measuring the acoustic impedance and temperature, respectively. For a more detailed explanation of the iDAS system, the reader is referred to [42].

Our fiber is coiled around a PVC pipe with a diameter of 0.125 m, which allows us to use more fiber and, hence, have more measuring points than when using a

straight fiber. In addition, the coining increases the vertical resolution by compressing the gauge length of 10 m of the cable (the length over which the back-scattered signal is averaged to increase the signal-to-noise ratio of the detected dynamic deformation) only over a few vertical centimeters. Due to the coiling, we also change the directional sensitivity [44], making the cable more sensitive to horizontal waves, with respect to the column. The PVC pipe with the fiber coiled on it is placed inside a transparent column. We first perform experiments with two types of synthetic clay, namely kaolinite and bentonite, and subsequently with two types of fluid mud – one from the Port of Rotterdam, which is the same sample mud as described above, and the other from the Port of Hamburg. For the experiments with the synthetic clays, we fill the lowest part of the column, without coiled optical fiber, with sand. Above the sand, we put one of the clays, and then we fill the remainder with water. For the fluid-mud experiments, we instrument also the lowest part of the column with fiber and start filling the column with one of the fluid muds starting already at the bottom, while we again fill the remainder of the column with water. A schematic overview and pictures of the setup are shown in **Figure 6**. Note that for the measurements with kaolinite and bentonite, we have 0.5 m in depth, which is 123 m in fiber length, acting as sensors. For the measurements in the muds, we added 0.2 m in depth, giving us a total of 171 m of fiber length, acting as sensors. For both setups, we have 10 m of fiber outside of our column to use as a reference.

With DAS, we try to capture the water/mud interface and measure the shear strength build-up. We test various sources for these purposes. Our sources include a small transducer with a center frequency of 500 kHz, a larger transducer with a center frequency of 200 kHz (**Figure 6b** and **c**) and a common duo echo-sounder with a center frequency of 38 kHz and 200 kHz, which is also used by marine vessels to measure depth. We connect these sources to the same source-side signal-control part as described above. We use a frequency range from 25 kHz to 45 kHz, since preliminary results indicated that this range should give the best results. The sampling frequency of the DAS system is set at the maximum of the system, which is 100 kHz.

For the DTS measurements, we use two standard heating rods, which we place 5 cm away from the fiber, to heat the column and measure the difference with respect to time along the column. This we only do for the kaolinite sample, since a very similar result is expected for the other clay and two mud samples.
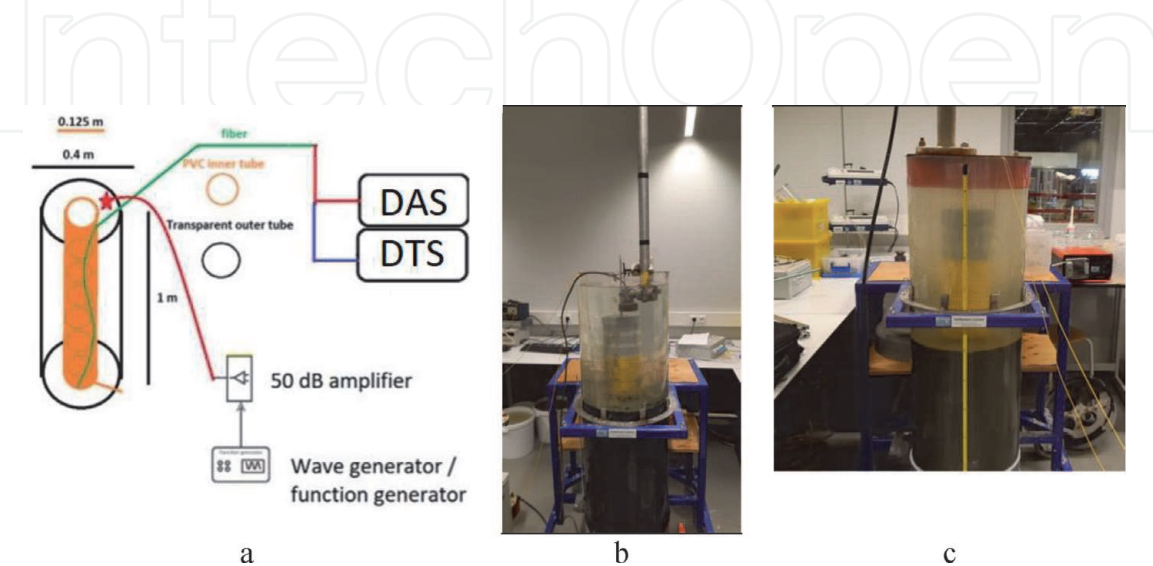

a   b   c

Figure 6.
(a) Schematic overview of the setup for DAS and DTS measurements. A photo of the column with the optical fiber wound around the PVC pipe when using mud from the (b) port of Rotterdam and (c) port of Hamburg.

3. Results

We describe the results of the ultrasonic transmission measurements with ultrasonic transducers and correlate them to the results from the rheological measurements. We further report the results from the reflection measurements and how they were used to retrieve ghost reflections. We then show the results from the DAS and DTS measurements.

3.1 P- and S-waves velocities in the fluid mud from transmission measurements with ultrasonic transducers

We examine the first arrivals of transmitted P- and S-waves and estimate their velocity variations during the consolidation of the fluid mud. We do not observe a detectable change in the P-wave velocity – the P-wave first arrivals appear to be constant throughout the consolidation process (**Figure 7a**). This finding agrees with previous results reporting that the S-wave velocity is more sensitive to changes in lithology and mechanical properties than the P-wave velocity [45]. The traveltime of the direct arrivals of the P-wave is 0.074 ms (**Figure 7a**), and thus the corresponding velocity is 1570 m/s. By examining the change in arrival time of the

Figure 7.
(a) Transmission recordings of the direct P- and S-wave arrivals as a function of consolidation time. (b) Estimated S-wave velocity as a function of the consolidation time.

first S-wave arrival (**Figure 7a**), we find that the S-wave traveltime decreases with consolidation time, indicating that the S-wave velocity increases with the consolidation progress (**Figure 7b**).

We can see from **Figure 7**, that during the first three days the S-wave velocity is nearly stable exhibiting very little fluctuations. Starting from Day 3, the S-wave velocity shows a strong increase from 959 to 995 m/s during the next two days. In the second week, the S-wave velocity only experiences a small increase and eventually reaches 998 m/s. By comparing the velocity variations of the P-wave and S-waves, we can summarize that the relative increase in the S-wave velocity is much stronger than in P-wave velocities, validating the statement that the S-waves are much more sensitive to the consolidation of the fluid mud than the P-waves. This finding agrees with a previous in-situ seismic exploration results using pulse-transmission techniques [45].

By drawing the estimated S-wave velocities from **Figure 7b** as a function of the concurrently estimated fluidic yield stresses (**Figure 8**), we see a positive correlation during the consolidation of the fluid mud. The correlation appears to indicate that the S-wave velocity starts increasing after the fluidic yield stress exceeds some critical value (for each of the Couette and vane geometry). Once the critical value is surpassed, the S-wave velocity increases with the increasing fluidic yield stress caused by the consolidation.

3.2 P- and S-wave velocities inside the fluid-mud layer from ghost reflections

The recorded primary reflections from the fluid-mud top and bottom are identified and shown in **Figure 9**. We apply SI using the reflection from the mud top in the CSG from S2 and the primary reflections PPPP, PPSP, and PSSP from the mud bottom in the CSG from S1 (**Figure 9**). As explained in Section 2.2, the ghost reflections are retrieved by eliminating the P-wave travel-paths inside the water. The ghost reflections in **Figure 10**, retrieved using the primary reflections PPPP, PPSP, and PSSP, are labeled PP, PS, and SS, respectively. In **Figure 10**, we also show the length of each of the legs of the reflection travel-paths of the retrieved ghost reflections. We use these lengths to estimate the wave velocities using the arrival times of the retrieved ghost reflections.
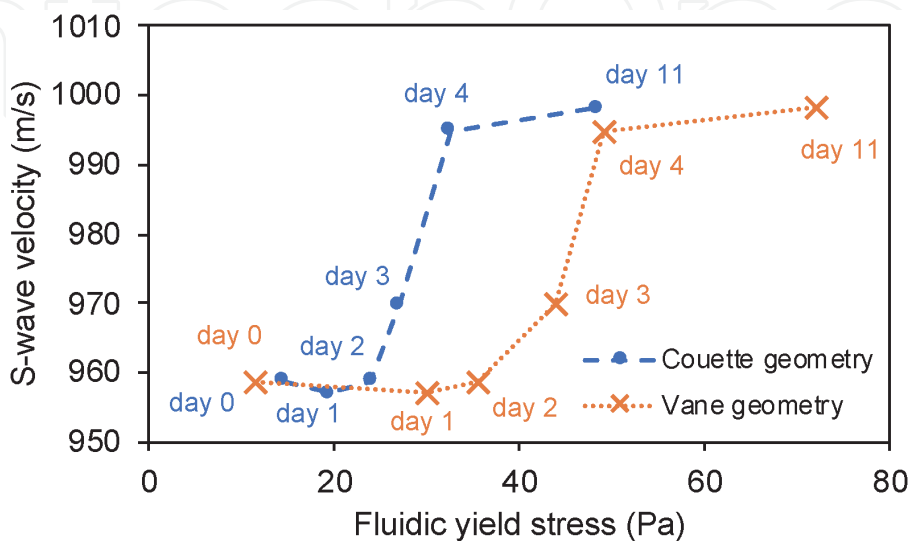

Figure 8.
*Relationship between the estimated S-wave velocities (**Figure 7b**) and the concurrently estimated fluidic yield stress, using Couette and vane geometry, as a function of the consolidation time.*
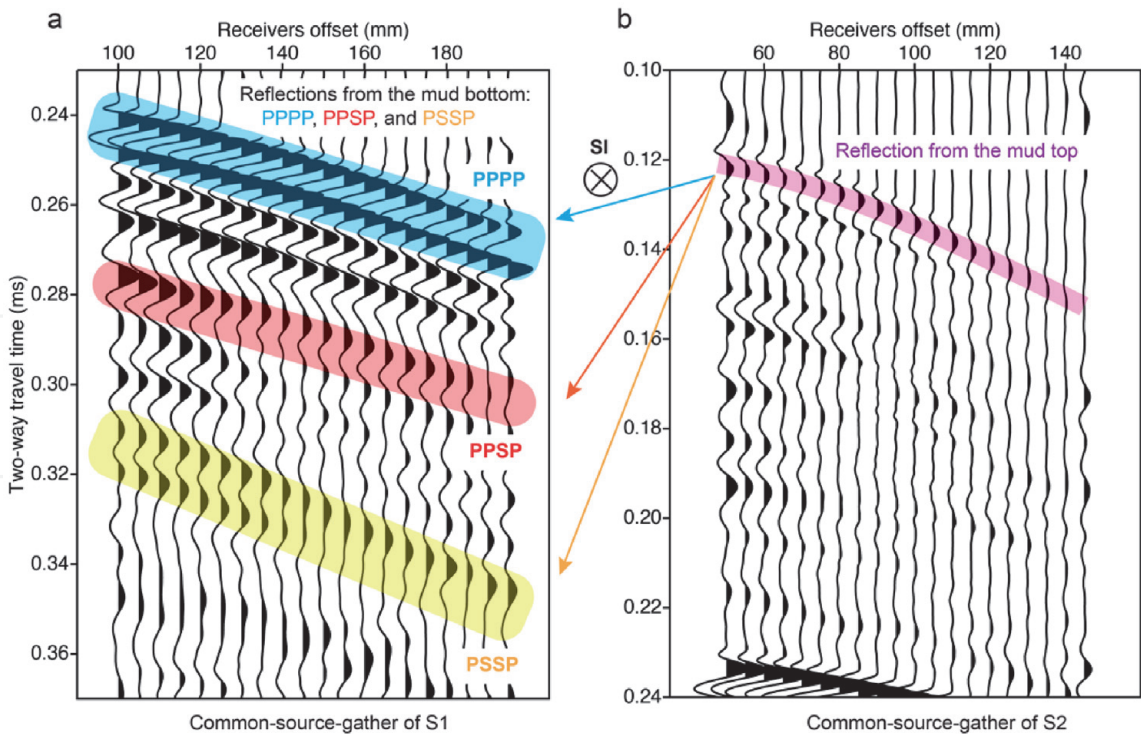
Figure 9.
Identified primary reflections in the common-source gather from (a) source 1 and (b) source 2. We apply seismic interferometry (SI) by correlating (the ⊗ symbol) the reflection from the mud top with each of the three identified reflections from the mud bottom followed by summation over the receivers (Eq. 3).
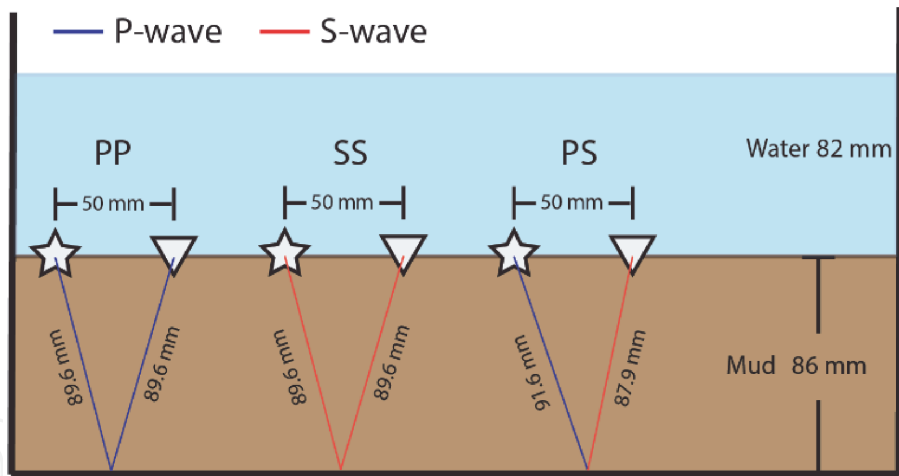

Figure 10.
The travel distances of the travel-paths of the ghost reflections PP, SS, and PS when the fluid-mud thickness is 86 mm, which is the thickness on day 11 of the consolidation.

As explained, the retrieved result is obtained by stacking the correlated traces. When the receiver array is sufficiently long, the stacking would have resulted in the retrieved ghost reflections only, with the contribution to the retrieved signal coming from summation inside the so-called stationary-phase region [46], i.e., the region where a curve appears nearly horizontal. In **Figures 11a–13a**, we indicate the stationary-phase regions with green dashed rectangles. Because our receiver array is of a limited length and is further only on one side of the sources, summation of all traces produces more or less erroneous results (**Figures 11b–13b**). Because of this, to retrieve the ghost reflections we use for the summation only traces in the stationary-phase region (**Figures 11c–13c**). We then pick from those results the two-way traveltimes to estimate the velocities inside the fluid-mud layer.
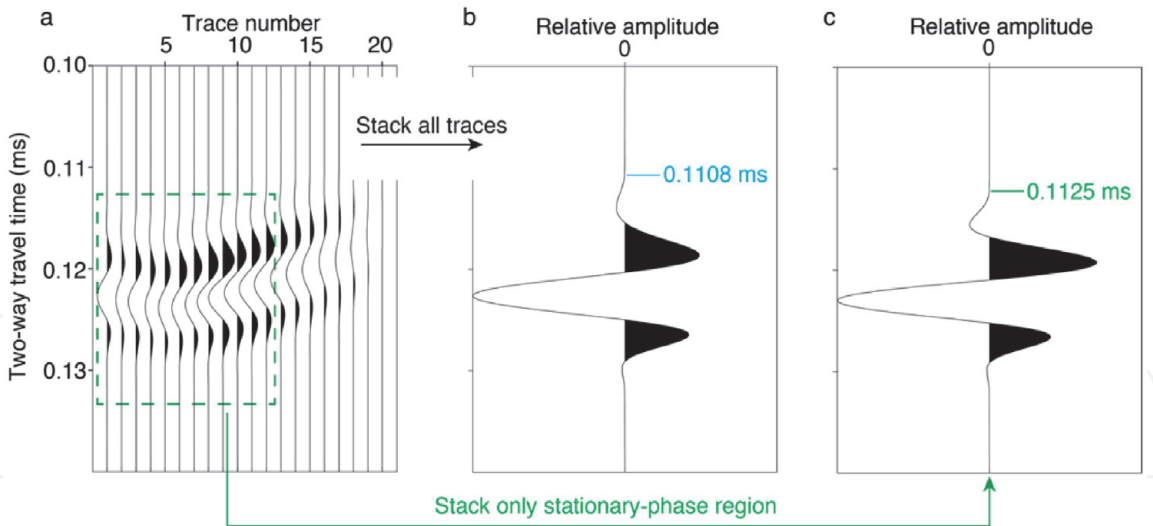
Figure 11.
*Two-way traveltime pick of the ghost reflection PP. (a) Correlation result of the reflection from the fluid-mud top from **Figure 9b** with the PPPP reflection from **Figure 9a**. The stationary-phase region is indicated by the dashed green rectangle. The retrieved ghost reflection PP when summing over (b) all traces in a and (c) the traces inside the stationary-phase region in a.*
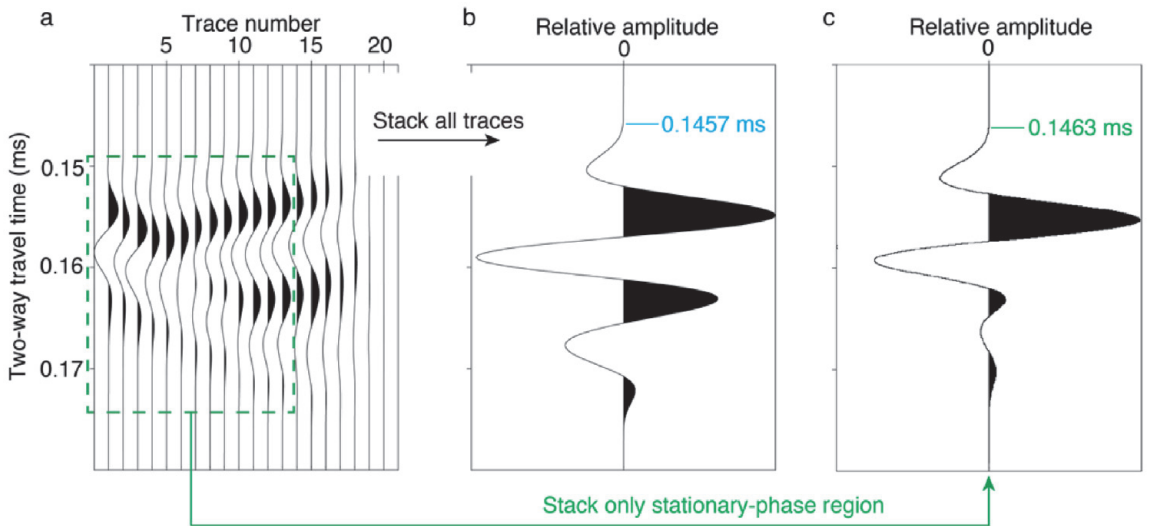

Figure 12.
*As in **Figure 11** but for ghost reflection PS. The correlation in (a) is with the PPSP reflection.*

Dividing the travel distance of 179.2 mm, which ghost reflection PP has traversed inside the fluid-mud layer (**Figure 10**) by the picked two-way traveltime from **Figure 11c**, we estimate the P-wave velocity to be 1592 m/s. To estimate directly the S-wave velocity inside the fluid-mud layer, we divide the travel distance the ghost reflection SS has traversed inside the fluid-mud layer, again 179.2 mm (**Figure 10**), by the picked two-way traveltime from **Figure 13c**, and obtain 995 m/s. Comparing this value with the estimated value from the transmission measurements on day 11 of 998 m/s (**Figure 7b**), we see that the difference is only 0.3%, which is negligible. Comparison of the estimated P-wave velocity to the value from the transmission measurements of 1570 m/s, we see that the difference is 1.4%, which is a bit higher but still acceptable.

3.3 Detection of the water/mud interface using DAS and DTS

Figure 14 shows DAS measurements of the arrivals recorded along the fiber as a function of arrival time when using the fluid mud from the Port of Hamburg and
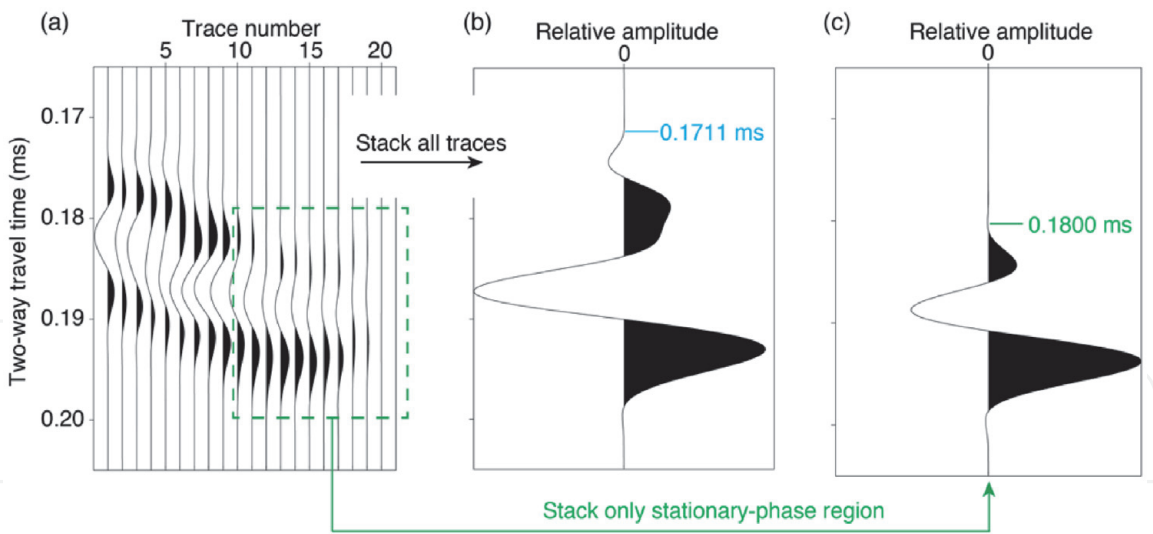
Figure 13.
*As in **Figure 11** but for ghost reflection SS. The correlation in (a) is with the PSSP reflection.*
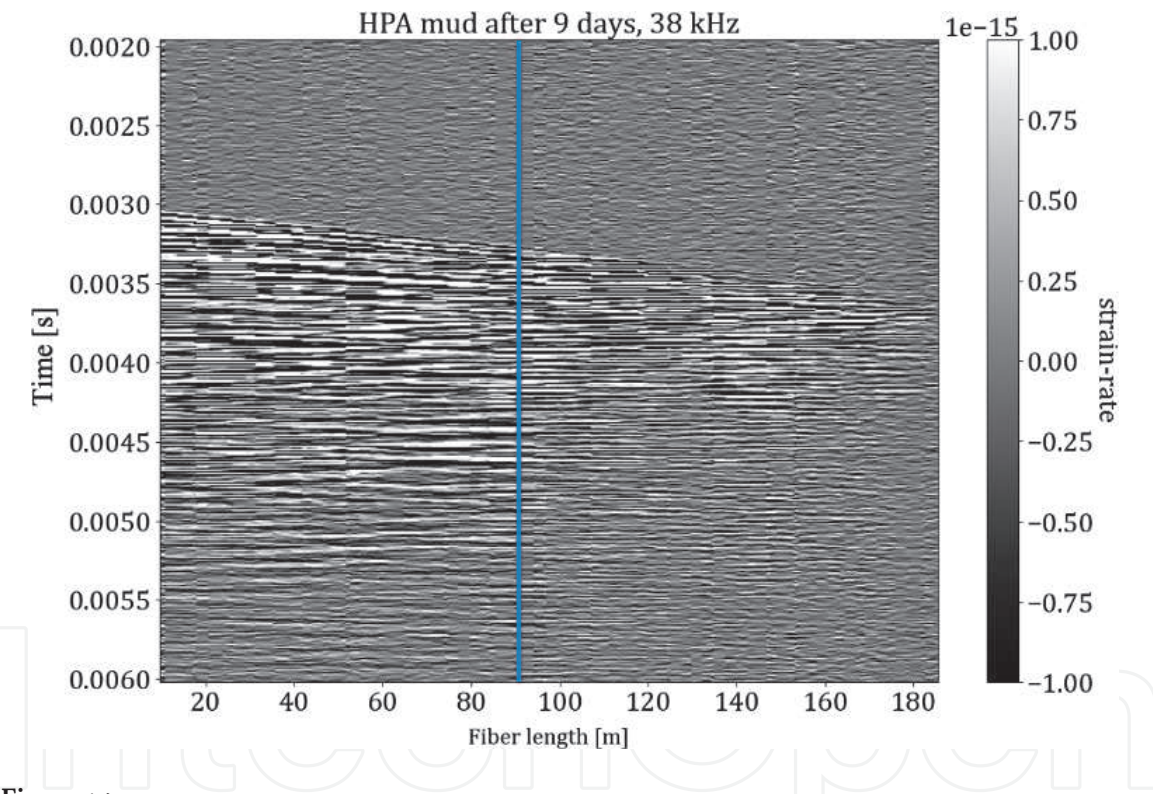

Figure 14.
*DAS recordings using the setup from **Figure 6c** showing direct arrivals and multiple reflections. The blue line indicates the water/mud interface, which is at 90.7 m along the fiber.*

the large transducer as a source (**Figure 6c**). We perform the measurements after the mud has consolidated for 9 days. To improve the signal-to-noise ratio, we repeat the recordings 10 times and then stack them. Using the first arrivals, i.e., the direct P-wave, we estimate the P-wave velocity in water to be around 1450–1500 m/s, while in the fluid mud to be 1490–1570 m/s. The reason for the uncertainty is likely related to the relatively low rate of time sampling of 100 kHz for the source frequency we use of 25–45 kHz. For this sampling rate, the Nyquist frequency is 50 kHz, which is very close to the source frequencies and, thus, makes the velocity analysis more ambiguous. The small difference in the P-wave velocity of the water and the fluid mud combined with the uncertainties make the detection of the water/ mud interface rather challenging if the first arrival as used.

The recordings in **Figure 14** show that a more accurate and robust criterion to detect the water/mud interface is to look at the multiple reflections and their amplitude attenuation. Looking at the figure, we can see that later arrivals appear to faint, i.e., are more attenuated after the water/mud interface, with the latter indicated by the blue line. Taking a closer look at the multiple reflections, we see that these later arrivals have completely fainted after 93.7 m fiber length, with the water/mud interface at 90.7 m fiber length. This difference of 3 m of fiber might be related to the gauge length of the fiber, i.e., the length over which the DAS system averages the observations, which in our case is 10 m. Another reason could be the uncertainty in the exact position of the fiber.

The measurements with the fluid mud from the Port of Rotterdam and the two clays show similar results.

We also look at the signal attenuation due to the consolidation of the mud, and thus the increase of its shear strength. **Figure 15a** and **b** show the DAS recordings in bentonite clay performed on the first and second day of the consolidation, respectively. We see a clear difference in signal penetration through the bentonite clay – on the first day, there is little to no signal penetration, opposed to the second day, when the waves propagate all the way through the column. This difference is purely related to the buildup of shear strength in the bentonite, since bentonite does not settle but builds up shear strength with time.

From the tests we perform with different types of sources (small and large transducer and duo echo sounder) we observe that the small transducer with resonant frequency of 500 kHz does not generate enough energy when we use it for emitting a P-wave at 25 kHz – 45 kHz. For that reason, it is outperformed by the big transducer whose resonant frequency of 200 kHz is closer to our target source-signal frequency of 25 kHz – 45 kHz. The duo echo sounder generated by far the strongest signal; however, because it was mounted on the transparent outer column and was situated right above our PVC pipe, a lot of tube waves and refracted waves are generated, which are undesired in our tests. These strong interfering events could potentially be suppressed applying further signal processing, as we suggest above – for example using a frequency-wavenumber filter.

Besides using the optical fiber as a receiver for seismic waves, we also use it as DTS recorder to measure temperature. Due to the difference in the heat capacity and heat conductivity between water and mud, a difference in heating occurs when we start heating up the column using heating rods in the water and kaolinite. This difference can be observed in **Figure 16**, where we show the measured Brillouin
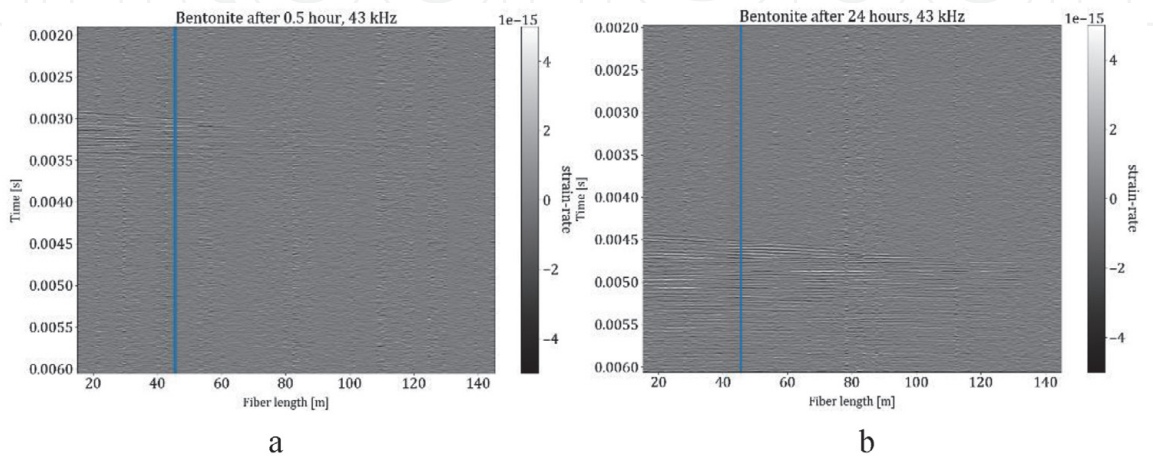

Figure 15.
DAS recordings when synthetic clay (bentonite) is used as fluid mud. The recordings were done after (a) half an hour and (b) 24 hours of consolidation of the bentonite.
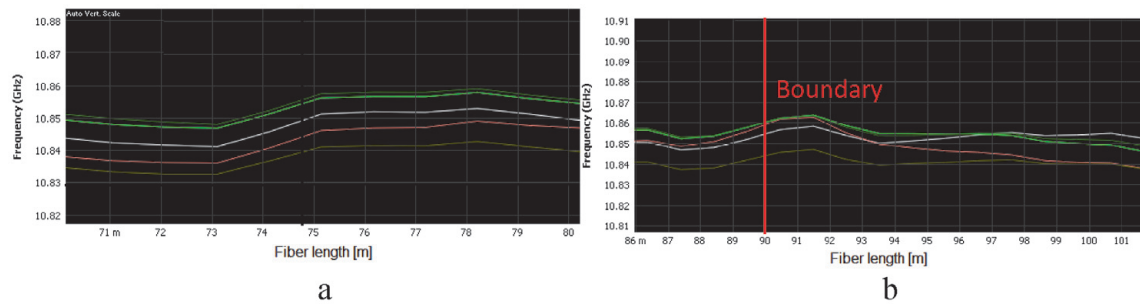
Figure 16.
Brillouin frequency changes in (a) water and (b) mud after increasing the temperature of the water in the column by 1°C. the red line indicates the water/mud interface. The brown curve represents a reference measurement without heating. The curves with colors other than brown represent measurements after heating up the water several times by 1°C.

frequency when we heat up the water and kaolinite. The brown curves show a reference measurement before the heating, while the other colored curves show the measurements after increasing the temperature of the water each time by 1°C. Inside the water layer (**Figure 16a**), we observe a linear increase in the Brillouin frequency per °C. Inside the mud layer, however, we see a non-linear trend due to the lower heat capacity and lower heat conductivity. This is especially visible along the red curve, which characterizes the first measurement after we start heating up the column: we see that in the lower part, starting at 99 m, the red curve overlaps the brown curve meaning that the heat from the heating rods has not yet reached the fiber at that level and deeper.

The DTS measurements show that interpretation of the water/mud interface can be achieved with a likely accuracy of around 4 cm.

4. Discussion

The direct transmission measurements of the P- and S-wave velocities inside the fluid-mud layer showed that the P-wave velocity is nearly independent of the consolidation process while the S-wave velocity significantly increases during the consolidation. This can be attributed to the property changes of the fluid mud due to the compaction effect of the consolidation and potentially the production of gas in the mud. The S-wave velocity is principally determined by the grain structure and shear modulus of the frame of the solid phase (minerals). The P-wave velocities on the other hand depend on the elastic moduli of the grains, sediment frame, and bulk modulus of the fluid. Thus, for marine sediments with high porosity, such as the fluid mud, the S-wave rather than the P-wave is strongly affected by the consolidation, and, thus, can be potentially used to characterize the consolidation process.

Using SI for retrieval of ghost reflections inside the fluid-mud layer, we removed the kinematic influence of the water layer above the mud. The estimated velocities of the P- and S-waves using the ghost reflections PP and SS, respectively, were very close to the ones estimated from the direct transmission measurements inside the fluid-mud layer. Because we also had the ghost reflection PS (**Figure 12**), we could estimate the S-wave velocity inside the fluid mud also from this arrival. We did this making use of the already estimated P-wave velocity for the propagation along the P-wave path of 91.6 mm in **Figure 10**. The value we then obtained was 991 m/s, which is quite close to the value of the S-wave velocity obtained from the ghost reflection SS, but is of course inheriting errors from the estimation of the P-wave velocity. Nevertheless, all three values can be used as quality control of each other

or as substitutes when one of the three ghost reflections cannot be reliably retrieved due to, for example, interference from other arrivals.

Observing the multiple reflections in the DAS recordings, we estimated an error of 3 m along the coiled fiber in detecting the depth of the water/mud interface. Since we coiled the fiber around a PVC pipe with a diameter of 0.125 m and because the fiber's thickness is 1.6 mm, the 3-meter error of fiber length translates to 1.2 cm of vertical error in the depth of the water/mud interface. With such an error, to the best of our knowledge, our approach is the most accurate non-intrusive method for determining the depth of the water/mud interface. Note that to achieve this accurate result, the only processing we applied was to increase the signal-to-noise ratio by the summation of the 10 separate recordings. More signal processing could further improve the determination of the water/mud interface. We expect that a similar high accuracy is achievable in the field as well since the upper end of the optical fiber is placed at the very bottom of the water layer, which limits errors caused by differences in, for instance, the water temperature.

The direct transmission measurements with DAS, on the other hand, allowed estimation of the P-wave velocity in the fluid mud in the range 1490–1570 m/s. Comparing these values to the value of 1570 m/s from the direct transmission measurements horizontally inside the fluid mud means an uncertainty of about 5.1%, which is not negligible. This confirms the difficulty when using a source in the water and receivers in the fluid mud, and clearly underlines the advantage of using SI with ghost reflections from reflection measurements. Thus, we argue that another very useful application of DAS could be with direct transmission measurements inside the fluid-mud layer, and thus also for transmission tomography between a vertical array of sources inside the mud and a vertical DAS pole with coiled fiber.

For our laboratory measurements, we used fluid-mud samples from the Port of Rotterdam and the Port of Hamburg. Nevertheless, our results and conclusions can be generalized to fluid-mud samples from other ports. Because the estimated P- and S-wave velocities using the ghost reflections do not depend kinematically on the water layer, this technique could easily be applied to any port or waterway. Of course, the P- and S-wave velocities of the fluid mud will differ from place to place, so those will need to be estimated for each place, for example for correlation with the yield stress. The DAS and DTS techniques for estimating the water/mud boundary can likewise be used at any other port or waterway, as they depend only on the strong contrast in the observed parameters between the layer and fluid-mud layer.

5. Conclusions

We presented recent results for non-intrusive characterization and monitoring of fluid mud in ports and waterways using ultrasonic measurements in transmission and reflection geometry, including measurements with Distributed Acoustic Sensing (DAS), and using temperature measurements with Distributed Temperature Sensing (DTS). We performed the measurements in a laboratory on samples from the Port of Rotterdam, Port of Hamburg, and two synthetic clays.

Using ultrasonic transmission measurements with transducers directly inside fluid mud, we investigated the changes in the velocities of longitudinal (P-) and transverse (S-) waves and their possible relation to the yield stress during the consolidation. We observed no detectable change of the P-wave velocities during the consolidation of the fluid mud. We observed that the S-wave velocities exhibited a relatively strong increase after the fluid mud settles for a certain amount

of time, in our study after 3 days. Comparing the estimated S-wave velocities to the concurrently estimated fluidic yield stress, we showed a positive correlation between the two. Our findings verify that the S-wave velocities increase with increasing yield stress caused by the fluid-mud consolidation and can thus be potentially used for indirect in-situ assessment of the yield stress.

Using ultrasonic reflection measurements with transducers, we investigated the direct estimation of the P- and S-wave velocities inside the fluid-mud layer. The source and receiver transducers were placed inside the water layer, but we showed that the kinematic influence of the water layer can be completely eliminated by retrieval of non-physical (ghost) reflections inside the fluid mud by application of seismic interferometry. Using the retrieved ghost reflections to estimate the layer-specific P- and S-waves velocities of the mud, we eliminated possible uncertainty due to salinity and temperature gradients of the water, which affect the velocity estimates using the usual seismic-reflection processing techniques. We show that the reflection-estimated velocities differ from the transmission-calculated values only by 1.4% and 0.3% for the P- and S-waves, respectively.

We also showed that DAS and DTS can be very effective in estimating the depth of the water/mud interface. We showed that a standard communication fiber is sufficient to achieve an accuracy in the estimated depth of the water/mud interface of 1.2 cm. This accuracy, to the best of our knowledge, is higher than what is achievable with any the currently used non-intrusive methods. Furthermore, we showed that the strength of the signal recorded with DAS is linked to changes in the shear strength of clays.

Acknowledgements

Conflict of interest

The authors declare no conflict of interest.

Author details

Deyan Draganov[1*], Xu Ma[1], Menno Buisman[1,2], Tjeerd Kiers[1], Karel Heller[1] and Alex Kirichek[1,3]

1 Faculty of Civil Engineering and Geosciences, Delft University of Technology, Delft, The Netherlands

2 Port of Rotterdam, Rotterdam, The Netherlands

3 Deltares, Delft, The Netherlands

*Address all correspondence to: d.s.draganov@tudelft.nl

IntechOpen

References

[1] McAnally WH, Friedrichs C, Hamilton D, Hayter E, Shrestha P, Rodriguez H, Sheremet A, Teeter A, ASCE task committee on Management of Fluid mud. Management of fluid mud in estuaries, bays, and lakes. I: Present state of understanding on character and behavior. Journal of Hydraulic Engineering. 2007 Jan;133(1):9-22.

[2] Harbour Approach Channels Design Guidelines. In: Report of Marcom Working Group. 2014. p. 49.

[3] Kirichek A, Chassagne C, Winterwerp H, Vellinga T. How navigable are fluid mud layers. Terra et Aqua: International Journal on Public Works, Ports and Waterways Developments. 2018;151.

[4] Delefortrie G, Vantorre M, Eloot K. Modelling navigation in muddy areas through captive model tests. Journal of marine science and technology. 2005 Dec 1;10(4):188-202.

[5] Vantorre M. Ship behaviour and control in muddy areas: state of the art. InProceedings of the 3rd International Conference on Manoeuvring and Control of Marine Craft (MCMC'94), edited by GN Roberts and MMA Pourzanjani, Southampton 1994 Sep (pp. 7-9).

[6] Claeys S, De Schutter J, Vantorre M, Van Hoestberghe T. Rheology as a survey tool: We are not there yet. Hydro International. 2011;15(3):14-19.

[7] Kirichek A, Rutgers R. Monitoring of settling and consolidation of mud after water injection dredging in the Calandkanaal. Terra et Aqua. 2020; 160: 16-26

[8] Kirichek A, Shakeel A, Chassagne C. Using in situ density and strength measurements for sediment maintenance in ports and waterways.

Journal of Soils and Sediments. 2020 Feb 19:1-7.

[9] Hamilton EL, Bachman RT. Sound velocity and related properties of marine sediments. The Journal of the Acoustical Society of America. 1982 Dec;72(6):1891-1904.

[10] Schrottke K, Becker M, Bartholomä A, Flemming BW, Hebbeln D. Fluid mud dynamics in the Weser estuary turbidity zone tracked by high-resolution side-scan sonar and parametric sub-bottom profiler. Geo-Marine Letters. 2006 Sep 1;26(3): 185-198.

[11] Gratiot N, Mory M, Auchere D. An acoustic Doppler velocimeter (ADV) for the characterisation of turbulence in concentrated fluid mud. Continental Shelf Research. 2000 Sep 10;20(12–13): 1551-1567.

[12] Meissner R, Rabbel W, Theilen F. The relevance of shear waves for structural subsurface investigations. InShear waves in marine sediments 1991 (pp. 41-49). Springer, Dordrecht.

[13] Shapiro NM, Campillo M. Emergence of broadband Rayleigh waves from correlations of the ambient seismic noise. Geophysical Research Letters. 2004 Apr 16;31(7).

[14] Wapenaar K, Fokkema J. Green's function representations for seismic interferometry. Geophysics. 2006 Jul;71 (4):SI33-SI46.

[15] Draganov D, Campman X, Thorbecke J, Verdel A, Wapenaar K. Reflection images from ambient seismic noise. Geophysics. 2009 Sep;74(5):A63-A67.

[16] Draganov D, Ghose R, Ruigrok E, Thorbecke J, Wapenaar K. Seismic

interferometry, intrinsic losses and Q-estimation. Geophysical Prospecting. 2010 Mar 26;58(3):361-373.

[17] Draganov D, Heller K, Ghose R. Monitoring CO2 storage using ghost reflections retrieved from seismic interferometry. International Journal of Greenhouse Gas Control. 2012 Nov 1;11: S35-S46.

[18] King S, Curtis A. Suppressing nonphysical reflections in Green's function estimates using source-receiver interferometrySuppressing nonphysical reflections. Geophysics. 2012 Jan 1;77 (1):Q15-Q25.

[19] Breitzke M. Acoustic and elastic characterization of marine sediments by analysis, modeling, and inversion of ultrasonic P wave transmission seismograms. Journal of Geophysical Research: Solid Earth. 2000 Sep 10;105 (B9):21411-21430.

[20] Leurer KC. Compressional-and shear-wave velocities and attenuation in deep-sea sediment during laboratory compaction. The Journal of the Acoustical Society of America. 2004 Oct;116(4):2023-2030.

[21] Ballard MS, Lee KM, Muir TG. Laboratory P-and S-wave measurements of a reconstituted muddy sediment with comparison to card-house theory. The Journal of the Acoustical Society of America. 2014 Dec;136(6):2941-2946.

[22] Ballard MS, Lee KM. Examining the effects of microstructure on geoacoustic parameters in fine-grained sediments. The Journal of the Acoustical Society of America. 2016 Sep 8;140(3):1548-1557.

[23] Collins JA, Sutton GH, Ewing JI. Shear-wave velocity structure of shallow-water sediments in the East China Sea. The Journal of the Acoustical Society of America. 1996 Dec;100(6): 3646-3654.

[24] Ajo-Franklin JB, Dou S, Lindsey NJ, Monga I, Tracy C, Robertson M, Rodriguez Tribaldos V, Ulrich C, Freifeld B, Daley T, Li X. Distributed acoustic sensing using dark fiber for near-surface characterization and broadband seismic event detection. Sientific Reports. 2019; 9:1328.

[25] Jousset P, Reinsch T, Ryberg T, Blanck H, Clarke A, Aghayev R, Hersir GP, Henninges J, Weber M, Krawczyk CM. Dynamic strain determination using fibre-optic cables allows imaging of seismological and structural features. Nature Communications. 2018; 9: 2509.

[26] Lindsey NJ, Martin ER, Dreger DS, Freifeld B, Cole S, James RS, Biondi BL, Ajo-Franklin JB. Fiber-optic network observations of earthquake Wavefields. Geophysical Research Letters. 2017 Dec 16; 44(23):11792-11799.

[27] Wang HF, Zeng X, Miller DE, Fratta D, Feigl KL, Thurber CH, Mellors RJ. Ground motion response to an ML 4.3 earthquake using co-located distributed acoustic sensing and seismometer arrays. Geophysical Journal International. 2018 Jun;213(3):220-236.

[28] Yu C, Zhan Z, Lindsey NJ, Ajo-Franklin JB, Robertson M. The potential of DAS in Teleseismic studies: Insights from the goldstone experiment. Geophysical Research Letters. 2019 Feb 16; 46(3):1320-1328.

[29] Daley TM, Miller DE, Dodds K, Cook P, Freifeld BM. Field testing of modular borehole monitoring with simultaneous distributed acoustic sensing and geophone vertical seismic profiles at Citronelle, Alabama. Geophysical Prospecting. 2016; 64(5): 1318-1334.

[30] Mateeva A, Lopez J, Potters H, Mestayer J, Cox B, Kiyashchenko D, Wills P, Grandi S, Hornman K, Kuvshinov B, Berlang W, Yang Z,

Detomo R. Distributed acoustic sensing for reservoir monitoring with vertical seismic profiling. Geophysical Prospecting. 2014; 62(4):679–692.

[31] Zeng X, Lancelle C, Thurber C, Fratta D, Wang H, Lord N, Chalari A, Clarke A. Properties of noise cross-correlation functions obtained from a distributed acoustic sensing Array at Garner Valley, California. Bulletin of the Seismological Society of America. 2017 Jan 31; 107(2):603-610.

[32] Ravet F, Rochat E, Niklès M. BOTDA-based DTS robustness demonstration for subsea structure monitoring applications. Proc. SPIE 9634, 24th International Conference on Optical Fibre Sensors. 2015 Sep 28; 96345Z.

[33] Stork AL, Chalari A, Durucan S, Korre A, Nikolov S. Fibre-optic monitoring for high-temperature carbon capture, utilization and storage (CCUS) projects at geothermal energy sites. First Break. 2020 Oct; 38(10):61-67.

[34] Shao M, Qiao X, Zhao X, Zhang Y, Fu H. Liquid level sensor using fiber Bragg grating assisted by multimode fiber core. IEEE Sensors Journal. 2016 Jan 7;16(8):2374-2379.

[35] Xu W, Wang J, Zhao J, Zhang C, Shi J, Yang X, Yao J. Reflective liquid level sensor based on parallel connection of cascaded FBG and SNCS structure. IEEE Sensors Journal. 2016 Nov 16;17 (5):1347-1352.

[36] Yang C, Chen S, Yang G. Fiber optical liquid level sensor under cryogenic environment. Sensors and Actuators A: Physical. 2001 Oct 31;94 (1–2):69-75.

[37] Wei M, McGuire JJ, Richardson E. A slow slip event in the south Central Alaska subduction zone and related seismicity anomaly. Geophysical Research Letters. 2012 Aug 16;39(15).

[38] Shizhuo Y, Ruffin PB, Francis TS. Fiber optic sensors. Talor & Francis Group. 2008;479.

[39] Shakeel A, Kirichek A, Chassagne C. Rheological analysis of mud from port of Hamburg, Germany. Journal of Soils and Sediments. 2020; 1-10.

[40] Shakeel A, Kirichek A, Chassagne C. Yield stress measurements of mud sediments using different rheological methods and geometries: An evidence of two-step yielding. Marine Geology. 2020; 106247.

[41] Draganov D, Hunziker J, Heller K, Gutkowski K, Marte F, high-resolution ultrasonic imaging of artworks with seismic interferometry for their conservation and restoration. Studies in Conservation. 2018; 63(5):277-291.

[42] Lindsey NJ, Rademacher H, Ajo-Franklin JB. On the broadband instrument response of fiber-optic DAS arrays. Journal of Geophysical Research: Solid Earth. 2020 Feb;125(2): e2019JB018145.

[43] Li W, Bao X, Li Y, Chen L. Differential pulse-width pair BOTDA for high spatial resolution sensing. Optics express. 2008 Dec 22;16(26):21616-21625.

[44] Kuvshinov B. Interaction of helically wound fibre-optic cables with plane seismic waves. Geophysical Prospecting. 2016; 64(3): 671–688.

[45] Ayres A, Theilen F. Relationship between P- and S-wave velocities and geological properties of near-surface sediments of the continental slope of the Barents Sea. Geophysical prospecting. 2001 Dec 24;47(4):431-441.

[46] Snieder R. Extracting the Green's function from the correlation of coda waves: A derivation based on stationary phase. Physical review E. 2004; 69(4): 046610.